Heliyon 7 (2021) e07633

Contents lists available at ScienceDirect

Heliyon

journal homepage: www.cell.com/heliyon

Research article

Graphene-based THz absorber: adjustability via multiple gate biasing

Sindokht Cyrus [a], Sadegh Biabanifard [b,*]

[a] Independent Researcher, Tehran, Iran
[b] Iran Analog Research Group, Tehran, Iran

ARTICLE INFO

Keywords:
THz
Absorber
Circuit model
Meta-material
Graphene disk
Multi-bias
Multi-layer

ABSTRACT

A multi-layer absorber using multi-bias arrays of graphene is proposed. The design methodology using the equivalent circuit model and matching concept is described. A heavy optimization process is performed to optimize bias values for different functionality. Leveraging, increased control parameters due to multi-bias scheme and simple circuit model representation, two operational modes are achieved as wide-band and multi-band absorption. The proposed absorber can perfectly absorb THz incident waves between 5.2 *THz* – 6.3 *THz* in wide-band mode while shows perfect absorption response in 5.3 *THz*, 7.5 *THz*, 8 *THz*, 8.5 *THz*, 9 *THz*, and 9.5 *THz*in multi-band operational mode. Besides, response dependency to layers thicknesses, electron relaxation time, chemical potentials, and incident angle are reported to express acceptable sensitivity of the device. Such a reconfigurable absorber is in demand for several applications, ranging from medical imaging to indoor communication.

1. Introduction

Terahertz (THz) spectrum gained extensive consideration in optical societies and engineering communities for emerging figure in numerus applications includes optical detection, non-destructive biosensing, medicine analysis, indoor high-speed communication and security. Operation in higher frequencies with smaller device size and lower photon energies are the major benefits of the THz frequency spectrum. Additionally, nanotechnology extensive growth in several academic and industrial fields mid presentation of novel extraordinary materials such as graphene, paved the way to highlight THz spectrum in modern electronics [1, 2]. The graphene as a two-dimensional material demonstrates magnificent plasmonic features compare to noble metals such as silver and gold [3, 4]. Also, the capability of adjusting the graphene conductivity by changing Fermi energy via external stimulation provides unique opportunity to design tunable or reconfigurable optical devices and systems. So, THz absorbers are in great demand for realizing optical systems. The absorber can assume as a basic cell for realizing numerus optical systems includes but not limited to sensors, solar devices, and processors. As a result, long listed researches have been reported different designs of THz tunable absorbers. Several geometries are studied as wave absorbers which most of them are metamaterials [5, 6, 7, 8, 9].

The presented wave absorbers in THz spectrum can be categorized in metallic structures, multi-layer dielectric-metal, graphene-dielectric-metal, multi-layer composites and cross-stacks structures in various geometries [10, 11, 12]. It should be mentioned that some presented structures are not feasible for fabrication while the configurations work only at specified frequencies. Additionally, it is not illustrated clearly how to design wave absorber at target frequencies with desirable absorption response. In this vision some scientists have tried to model the physical structures via passive circuit elements to provide more degree of freedom against conventional modeling [13, 14].

Most of the previous works provide numerical simulations as reference for design validation. While recent work in [4] provides an exclusive circuit representation for graphene patterns include periodically arrays of graphene ribbons and disks. So, turning design to a straight forward circuit matching can pave the path to more speedy design [15, 16]. Focusing on feasible patterns, nano-ribbons and nano-disks are more common among other graphene shapes. In this way [17, 18], present ultra-broadband absorbers with conventional periodic graphene nano-ribbons and nano-disks. The idea behind, stems from the fact that each layer excites localized plasmons. Also [19, 20], proposed multi-band absorbers with high adjustability via chemical potentials. These structures suffer from intensive sensitivity to design geometries. Also, all of these works use a single bias for a single layer. This limits control ability severely since chemical potential values cannot exceed

* Corresponding author.
E-mail address: biabani.sadegh@gmail.com (S. Biabanifard).

https://doi.org/10.1016/j.heliyon.2021.e07633
Received 13 January 2021; Received in revised form 31 May 2021; Accepted 19 July 2021

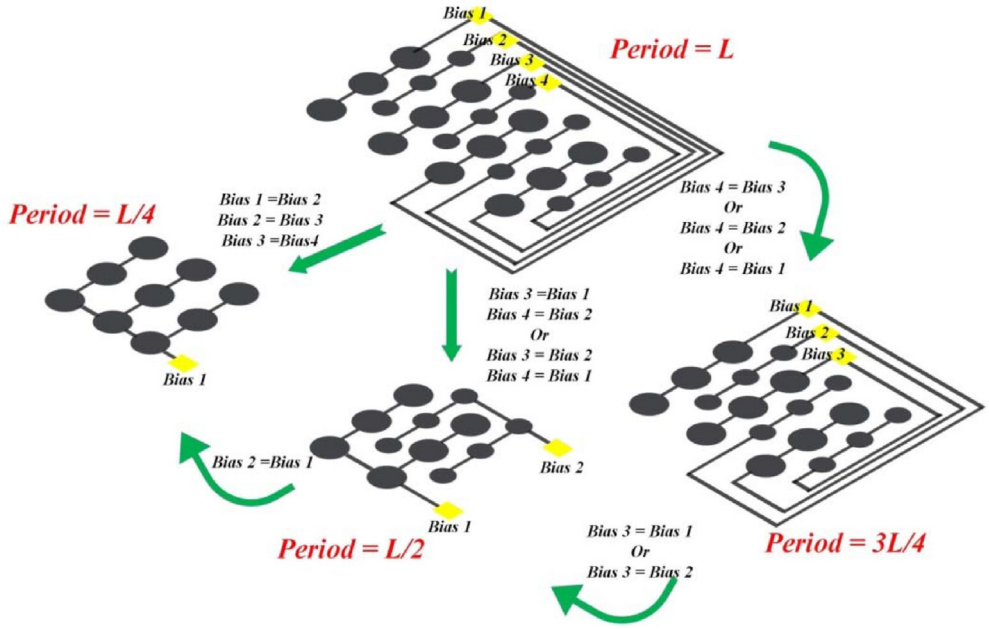

Figure 1. Introducing a multi-bias pattern using graphene nano-disks. The presented pattern is modeled differently depends on bias equalities. In this way by setting bias values, the pattern is forced to experience specified period values as illustrated in the figure.

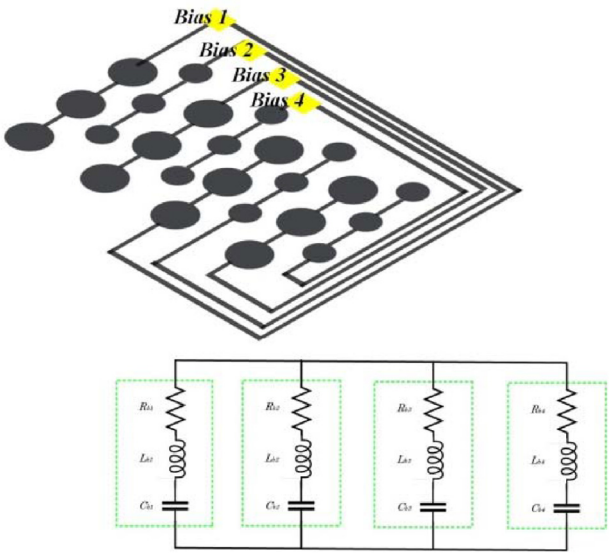

Figure 2. A four bias graphene pattern with its corresponding ECM representation.

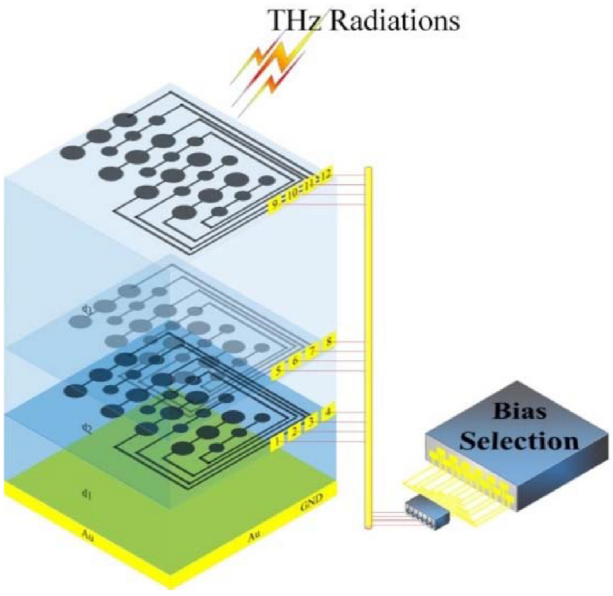

Figure 3. The proposed device consisting of three layers of nano-disks graphene over the TOPAS polymer. The total layers are set over a golden surface to ensure zero transmission. The shown bias scheme is symbolic. In reality direct contact via graphene bridges or placing the graphene layer between two ionized gel layers are common ways to bias the graphene patterns.

more than 1 eV, otherwise, chemical reactions occur. This may relate to the ultra-thin layer of graphene [21].

Albeit, the need of a comprehensive analytical design approach is felt which provides desirable absorption response at target THz frequencies. This work tries to express an accurate design methodology for reconfigurable absorbers over THz spectrum. Additionally, exploiting multiple gate biasing scheme besides impedance matching concept to achieve tunable and perfect absorption are discussed. The presented structure in this work is highly insensitive to polarity while benefits from wide angle absorption. Moreover, the developed equations to model graphene-based absorbers for graphene nano-disks are provided from [22] and [23].

The paper is arranged to explain proposed approach in section 2 which increase the control ability of the device as a multi-bias scheme. The idea behind the multi-bias scheme is explained and developed. Equivalent states are discussed to a more in-depth vision. This section introduces a new biasing scheme that can affect the structure like a geometrical parameter. This phenomenon is used to reach a desirable response. Section 3 presents the proposed device as a three-layer structure with twelve biases. Each layer includes four possible chemical potentials that can form a desirable reaction against incident THz waves. The equivalent passive circuit representation is explained in section 3. The proposed procedure has expressed in section 4, step by step in detail. This section considers feasible assumptions for a practical design. Additionally, the optimization process via a developed Genetic Algorithm (GA) is explained in section 5. This section describes defined cost-functions and exploited mutation to find optimum bias values. Ample

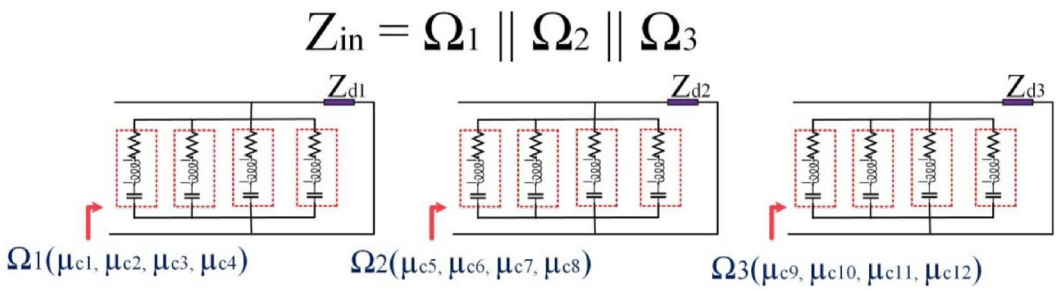

Figure 4. Equivalent circuit representation of proposed structure. To a more simplified vision, the circuit representation is divided into three similar parts.

Table 1. Eigenvalues of Eq. (10) [4].

$\frac{2a}{L}$	0.1	0.2	0.3	0.4	0.5	0.6	0.7	0.8	0.9
$q_{11}a$	0.539	0.536	0.533	0.530	0.527	0.499	0.472	0.444	0.417

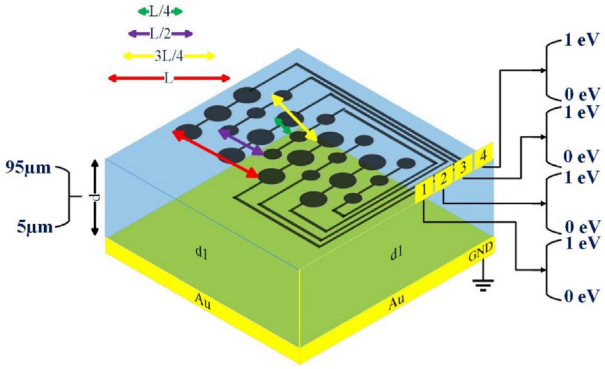

Figure 5. The single layer of the proposed structure with its probable characteristics. The thickness can set from 5μm to 95μm. The pattern period can change between four possible values and the chemical potentials can vary between 0 eV to 1 eV. The final values are optimized using a GA.

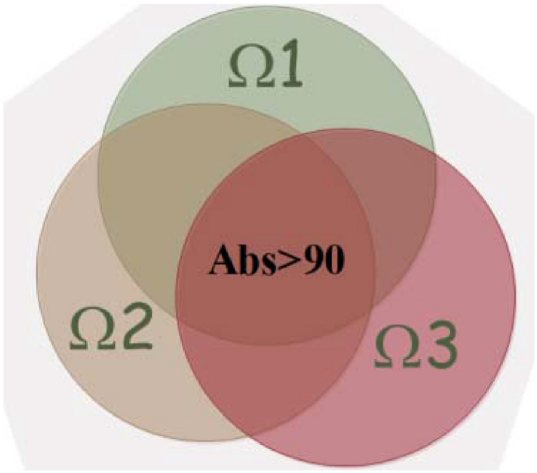

Figure 6. Symbolic representation of target input impedance. Recalling Figure 4, the structure impedance is the total value of paralleling Ω_1, Ω_2, and Ω_3.

simulation results are reported in section 6. Extracted absorptions via the Finite Element Method (FEM) and Equivalent Circuit Model (ECM) are reported in section 6. Also, device sensitivity versus layers thicknesses and chemical potentials are discussed to validate the reliability of the proposed device. Finally, conclusion is stated in section 7.

2. Proposed approach

Introducing a multi-bias scheme as depicted in Figure 1, can cause numerus possible behaviors versus radiation waves. Important and interesting exclusivity is the capability of changing external voltages to tune the response. In this way, if all four biases are equal, the pattern turns to a conventional layer with one gate bias. The only difference in the geometrical point of view is the modified disks period. In this case (Figure 1), the period (L) can vary to a quarter, three quarters, and half of the original value. So, biases equalities affect the device in a way that a geometrical parameter (L) changing. This is very interesting since geometrical aspects cannot vary after fabrication, but external biases can easily change. Additionally, biases values can control the impedances of layers, help to adjust input impedance to be matched with free space impedance equal to a real value of $120\pi\Omega$. Also, it should be noted that biases numbers can be extended more, but it may cause huge complexity to deal with. So, in this work we assume a four biases pattern to design a reconfigurable absorber. The corresponding circuit model is depicted via Figure 2. According to this figure, each bias shows a single RLC branch. Passive elements values (R, L, C) are quite specified by knowing geometrical values, physical constants, and chemical potential value. So, using the multi-bias pattern allows raising control ability over impedance value. This is a great potential to satisfy impedance matching theory which is the goal of the design.

Figure 7. The GA structure.

Table 2. Forming an initial population.

$Individual_1$	μ_{c1-1}	μ_{c2-1}	μ_{c3-1}	μ_{c4-1}	d_1
$Individual_2$	μ_{c1-2}	μ_{c2-2}	μ_{c3-2}	μ_{c4-2}	d_2
$Individual_3$	μ_{c1-3}	μ_{c2-3}	μ_{c3-3}	μ_{c4-3}	d_3
.	.	.	.	.	.
.	.	.	.	.	.
.	.	.	.	.	.
$Individual_{n-1}$	$\mu_{c1-(n-1)}$	$\mu_{c2-(n-1)}$	$\mu_{c3-(n-1)}$	$\mu_{c4-(n-1)}$	d_{n-1}
$Individual_n$	μ_{c1-n}	μ_{c2-n}	μ_{c3-n}	μ_{c4-n}	d_n

Table 3. Performing cross over operation.

$Individual_1$	μ_{c1-1}	μ_{c2-1}	μ_{c3-1}	μ_{c4-1}	d_1
$Individual_2$	μ_{c1-2}	μ_{c2-2}	μ_{c3-2}	μ_{c4-2}	d_2
$Individual_3$	μ_{c1-3}	μ_{c2-3}	μ_{c3-3}	μ_{c4-3}	d_3
$Individual_{new}$	μ_{c1-2}	μ_{c2-2}	μ_{c3-1}	μ_{c4-3}	d_3

Table 4. The Mutation Process (a random gene is selected and multiplied with a random number between 0 to 1).

i^{th} individual	μ_{c1i}	μ_{c2i}	**μ_{c3i}**	μ_{c4i}	d_i
			⬇		
i^{th} individual	μ_{c1i}	μ_{c2i}	**μ_{c3i} (mutated)**	μ_{c4i}	d_i

Table 5. Geometry values of the proposed reconfigurable absorber.

	First Layer	Second Layer	Third Layer
Designed Absorber Geometry	a = 18.2 μm L = 57 μm d_1 = 25 μm	a = 39.6 μm L = 112.85 μm d_2 = 13 μm	a = 39.6 μm L = 112.85 μm d_3 = 23 μm

Table 6. The chemical potentials values for two operational modes.

Parameters	Mode A	Mode B
μ_{c1} (eV)	0.45	0.65
μ_{c2} (eV)	0.45	0.05
μ_{c3} (eV)	0.03	0.25
μ_{c4} (eV)	0.15	0.45
μ_{c5} (eV)	0.65	0.55
μ_{c6} (eV)	0.25	0.65
μ_{c7} (eV)	0.05	0.25
μ_{c8} (eV)	0.25	0.15
μ_{c9} (eV)	0.45	0.05
μ_{c10} (eV)	0.36	0.15
μ_{c11} (eV)	0.05	0.65
μ_{c12} (eV)	0.03	0.05
τ (ps)	0.1	0.1

The next section proposes the absorber structure using a multi-bias scheme.

3. Proposed device

Figure 3 shows the proposed reconfigurable wave absorber. The device includes three layers. Each layer consists of four biases graphene nano-disks over a dielectric.

Thermoplastic Olefin Polymer of Amorphous Structure (TOPAS) is used as dielectric. The corresponding refractive index for TOPAS is $n_{TOPAS} = 1.53$, while this polymer express negligible losses at THz frequencies [24]. Besides a relatively thick golden surface is placed at the bottom of the device to ensure banned transmission. The thickness of the golden plate has to be comparable with penetration depth of radiated THz waves, about a few μm (in this case 2 μm). In addition, the gold surface conductivity is assumed equal to $4 \times 10^7 \frac{1}{\Omega m}$. As illustrated by Figure 3, the device has twelve biases. Several sets of bias values can be applied to the device. The main question is how to find these biases values following a desirable response which is answered in the next section.

In accordance to Figure 4, a single bias graphene nano-disks is equivalent to $R-L-C$ in cascade configuration while dielectric expresses a pure imaginary impedance. The missing part is equivalent circuit representation for golden surface which is assumed as simple short circuit. Figure 4 considers the layer's circuit model separately for simplicity. All three parts are assumed parallel to the model whole device circuit model.

Two terms contribute to form graphene conductivity, the intra band and inter band ($\sigma_G = \sigma_{intra} + \sigma_{inter}$) [4]. By knowing that $\hbar\omega << 2\mu_c$, the intra band becomes dominant term, so, surface conductivity of graphene can be written by Eq. (1) [4]:

$$\sigma_g(\omega, \mu_c, \tau, T) = -j\frac{e^2 k_B T}{\pi\hbar^2(\omega - j\tau^{-1})} \times \left[\frac{\mu_c}{k_B T} + 2\ln\left[\exp\left(-\frac{\mu_c}{k_B T}\right) + 1\right]\right] \quad (1)$$

where:

e : Electron charge and is equal to $1.62 \times 10^{-19}\frac{C}{J}$

K_B : Boltzmann constant and is equal to$1.38 \times 10^{-23}\frac{m^2\ kg}{s^2\ K}$.

τ: The relaxation time and here is equal to1 ps.

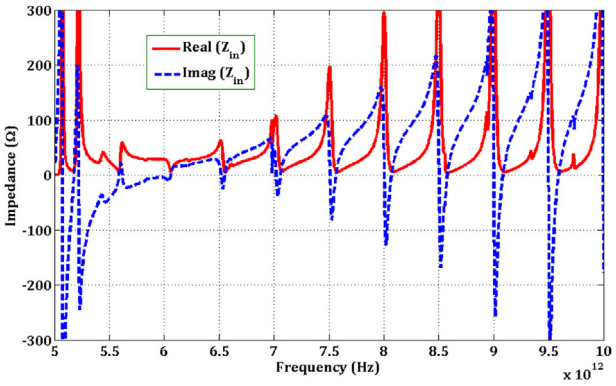

Figure 8. Calculated both real and imaginary sections for input multi-band mode (Mode A).

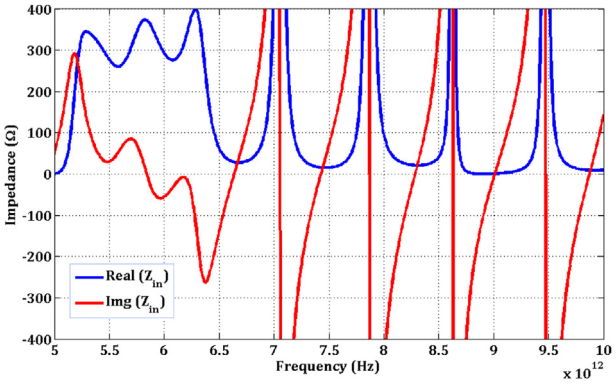

Figure 9. Calculated both real and imaginary sections for input wide-band mode (Mode B).

T: The temperature room and is equal to300 K.
μ_c: The chemical potential.

Also, to model dielectric as an impedance, Eq. (2) is presented. This impedance is based on load, thickness and output referred impedance. It should be noted that in accordance to Figure 6, Z_1 experiences short circuit at the end of the line. As a result, Eq. (2) turns to Eq. (3) if $Z_L = 0$ that means short circuit load. Consequently, dielectric impedance is presented by Eq. (3) [8]. Additionally, Eqs. (4), (5), (6), (7), (8), and (9) describe impedance calculation for proposed structure.

$$Z_{in} = R_0 \frac{Z_L + jR_0.\tan(\beta_d d)}{R_0 + jZ_L.\tan(\beta_d d)} \tag{2}$$

$$Z_{in} = jX_{is} = jR_0.\tan(\beta_d d) \tag{3}$$

$$Z_{d1} = jz_d.\tan(\beta_d d_1) \tag{4}$$

$$\Omega_1 : Z_{d1} \| Z_{g1} = \frac{z_{d1}.z_{g1}}{z_{d1} + z_{g1}} \tag{5}$$

$$Z_{d2} = jz_d.\tan(\beta_d d_2) \tag{6}$$

$$\Omega_2 : Z_{d2} \| Z_{g2} = \frac{z_{d2}.z_{g2}}{z_{d2} + z_{g2}} \tag{7}$$

$$Z_{d3} = jz_d.\tan(\beta_d d_3) \tag{8}$$

$$\Omega_3 : Z_{d3} \| Z_{g3} = \frac{z_{d3}.z_{g3}}{z_{d3} + z_{g3}} \tag{9}$$

where:

$Z_d = \frac{Z_0}{n_p}$ The dielectric impedance.
β_d The propagation constant of the THz wave in the dielectric.
Z_{g1}, Z_{g2}, and Z_{g3} the graphene patterns impedance.

Additionally, the modeled resistor, inductor, and capacitor of the nth order mode for periodic nano-disks are reported via Eq. (10) [4]:

$$R_n = \frac{K_n L^2}{\pi S_n^2} \frac{\eta^2}{e^2 E_F \tau}, \quad L_n = R_n \tau, \quad C_n = \frac{\pi^2 S_n^2}{L^2 K_n} \frac{\varepsilon_{eff}}{q_{11}} \tag{10}$$

where:

$\varepsilon_{eff} = \frac{\varepsilon_1 + \varepsilon_2}{2}$ is the permittivity of dielectric materials which surrounded the graphene layer on both sides.
q_{11} is dependent of radius and period of disks (a,L) and extracted from Table 1 [4]:

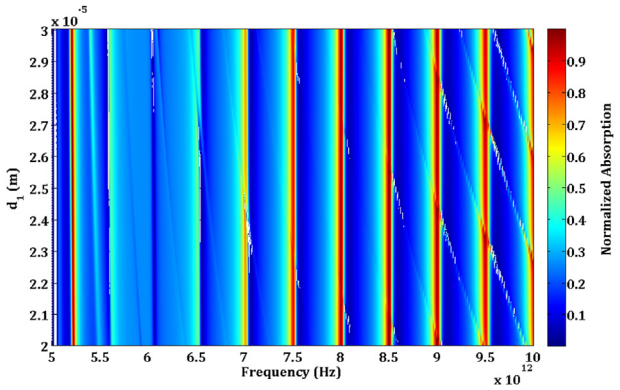

Figure 11. Absorption against a 10 % variation of first layer thickness for multi-band mode (Mode A).

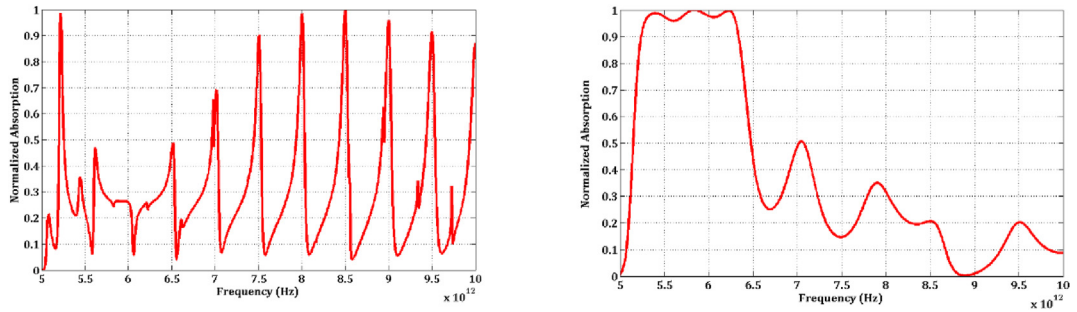

Figure 10. Absorption response. Left: Multi-band absorption. Right: Wide-band absorption.

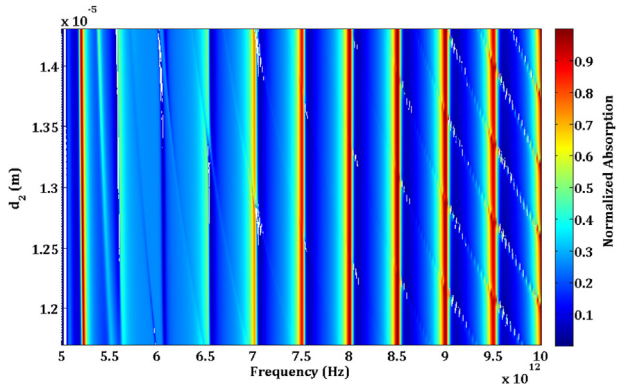

Figure 12. Absorption against a 10 % variation of second layer thickness for multi-band mode (Mode A).

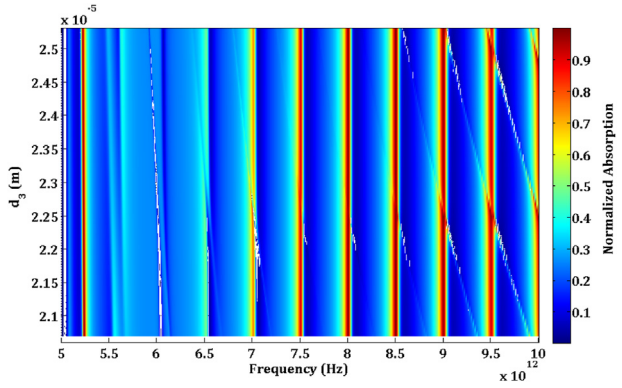

Figure 13. Absorption against a 10 % variation of third layer thickness for multi-band mode (Mode A).

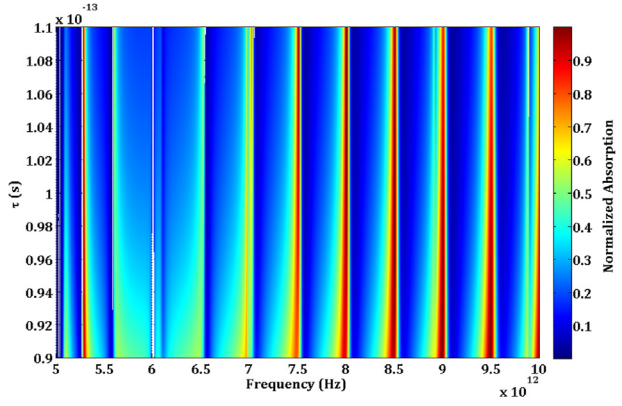

Figure 14. Absorption against a 10 % variation of electron relaxation time for multi-band mode (Mode A).

S_n is the integral of the Eigenfunctions of Eq. (10) and here for simplicity just first mode is considered (S_1) and is equal to $0.6087a$, while,.$K_1 = 1.2937$

According to the mentioned description, now we can calculate the referred structure impedance. The impedance predicts device behavior versus frequency and can be used to completely model the proposed device.

4. Design methodology

Considering real fabrication constraints, we assumed graphene patterns in a fixed geometry. It guarantees compliance with technology

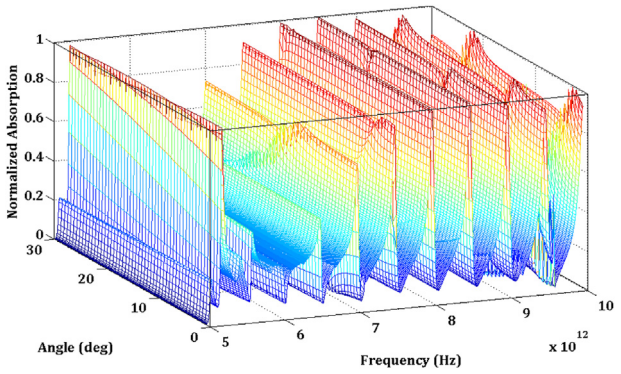

Figure 15. Absorption against different angles of the incident wave for multi-band mode (Mode A).

availabilities. So, the concentration turns to bias values. In this way assuming equal biases values for multi-bias patterns turns it to a conventional pattern with a decreased repeating period. This behavior can be considered as L tuning in specified values. If we assume L as a geometrical parameter, so we have found a way to manipulate geometry with the aim of external voltages while the physical structure is intact. This is important since the only reliable control parameters are chemical potentials of graphene patterns while the structure is fixed and cannot be modified physically. As a conclusion, finding disks radius and period is the first step. This step may limit numerous possibilities but to be compliant with technology, it is necessary. Otherwise, several geometries may lead to extra-ordinary results which are not feasible for fabrication. The simplest way is to consider disks radius and period based on previous works. This step can be reconsidered for further process. For example, a pre-stage optimization may help to improve the whole response. But here in this work, we fixed the disk radius according to [13]. If we consider geometrical parameters known, the result is that the structure impedance is related to dielectrics thicknesses and chemical potentials. Generally, as shown in Figure 3, the proposed device is a function of twelve chemical potentials (μ_{c1}, μ_{c2}, μ_{c3}, μ_{c4}, μ_{c5}, μ_{c6}, μ_{c7}, μ_{c8}, μ_{c8}, μ_{c9}, μ_{c10}, μ_{c11}, and μ_{c12}) and three thicknesses (d_1, d_2, and d_3). As we know graphene patterns are fixed. So, we are dealing with a problem with fifteen variables. It can be simpler if some biases are set equal to each other. For example, if we consider single-bias value for each layer, the problem has six variables to be optimized (three chemical potentials and three-layer thickness). Regardless of variable numbers, such a complex and non-linear problem cannot be solved via paper and pencil. So, exploiting an evolutionary algorithm is inevitable. In this regard, Figure 5 is drawn to show the scenario for single-layer design. In our defined scenario, variable parameters are chemical potentials, pattern period, and dielectric thicknesses. Chemical potentials can vary between 0eV to 1eV, while dielectric thickness varies from 5μm to 95μm. Also disks period can switch between four possible values depends on biases equalities.

5. The evolutionary algorithm

The proposed structure in Figure 3 consists of a relatively large number of parameters. Twelve chemical potentials, three layers thicknesses, and twelve radiuses of disks. For simplicity, we assume disks radiuses equal for each layer. Additionally, to reduce computational time and effort, each layer is processed separately. The total input impedance is a parallel configuration of all three parts. If we looking for absorption larger than 90 %, so each layer can show a probable impedance range as shown in Figure 6. The corresponding chemical potentials and layer thickness which lead to the target impedance range are outputs of the exploited GA. In this way, a GA consists of five parts based on Figure 7 is developed. As mentioned, this algorithm searches for optimal chemical potentials and layer thicknesses to force the structure to be matched with

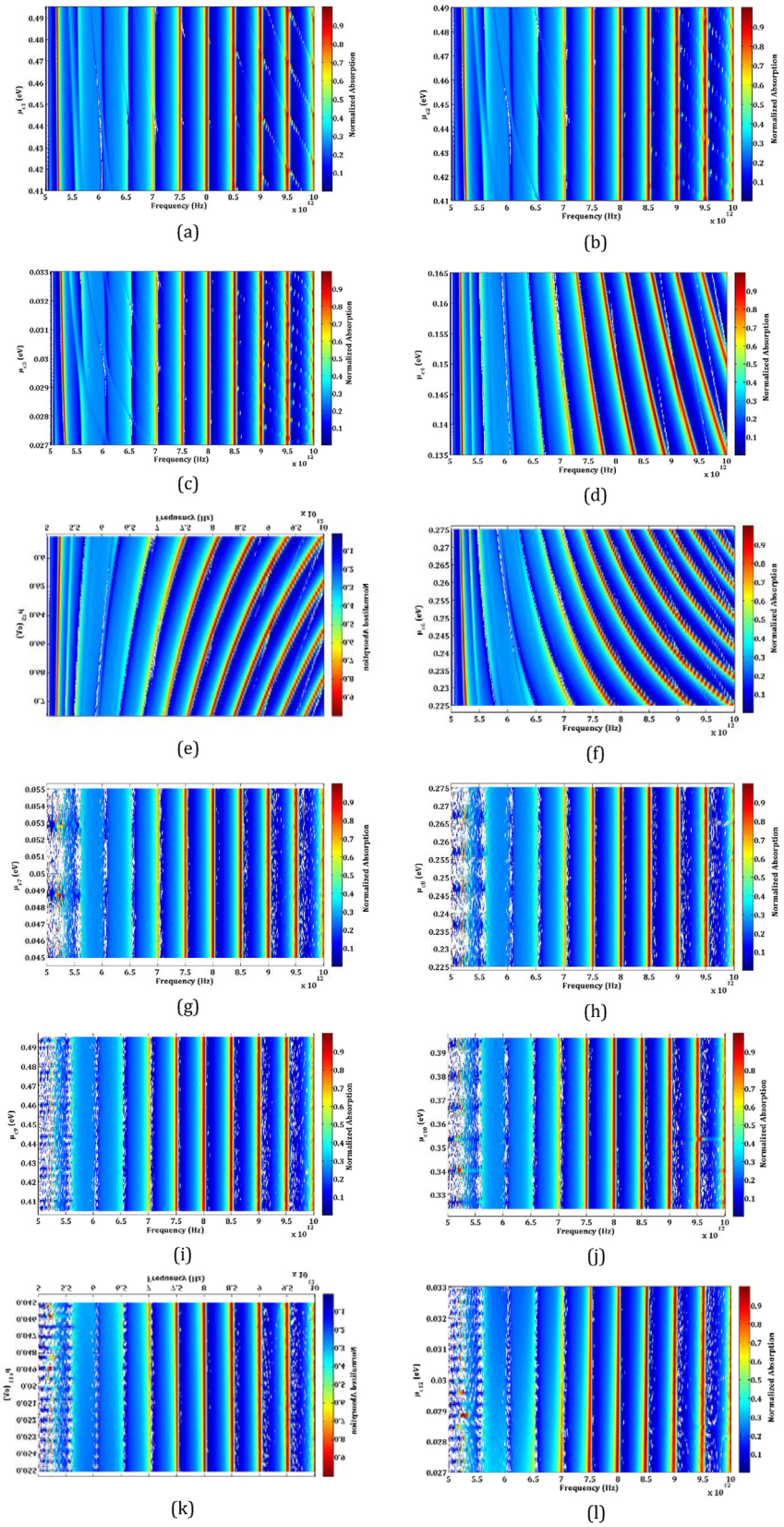

Figure 16. Absorption for 10 % variations of chemical potentials for multi-band mode (Mode A). Sub-Fig. (a) to Sub-Fig. (l) show absorption for μ_{c1} to μ_{c12} variations respectively.

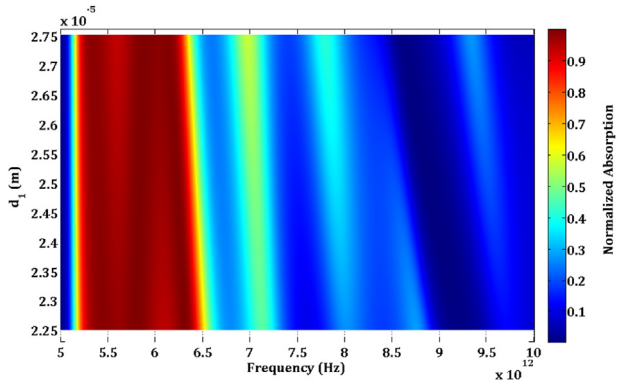

Figure 17. Absorption against 10 % variations of first layer thickness for wide-band mode (Mode B).

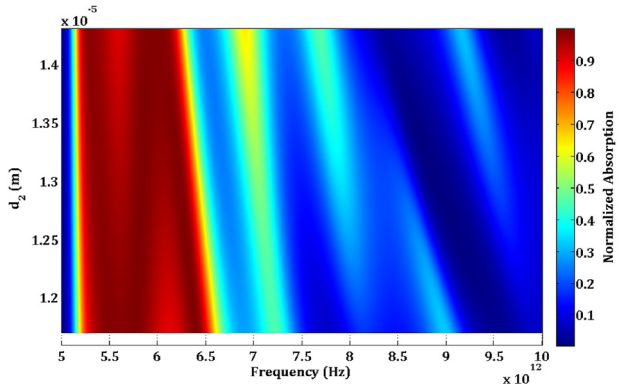

Figure 18. Absorption against 10 % variation of second layer thickness for wide-band mode (Mode B).

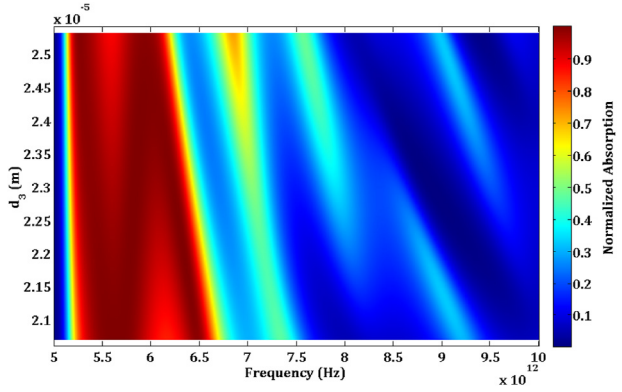

Figure 19. Absorption against 10 % variation of third layer thickness for wide-band mode (Mode B).

free space. The procedure begins with forming an initial population, producing new generation by cross over the operation, and finishes by satisfying defined cost functions. Additionally, mutation action is included to ensure escaping from relative maximums. And finally, it should be noted that the whole algorithm works to satisfy the impedance matching concept. This means that the ideal impedance of the proposed device must shows zero for imaginary and 120 π Ω for real part.

5.1. Forming the initial population

To start the optimization process, we need an initial population. Table 2 shows a symbolic generation of the population for a single layer with five genes as five design variables. Population size (n) is important

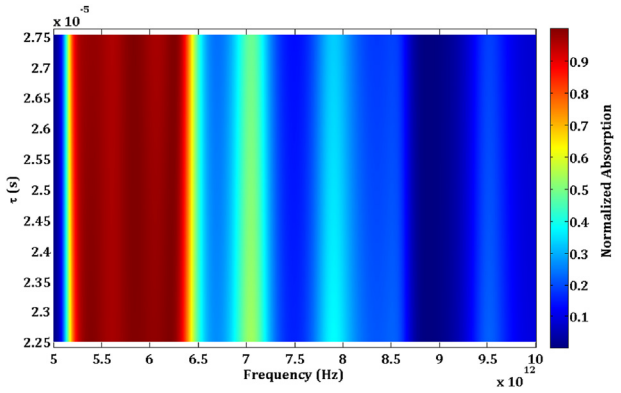

Figure 20. Absorption against 10 % variation electron relaxation time for wide-band mode (Mode B).

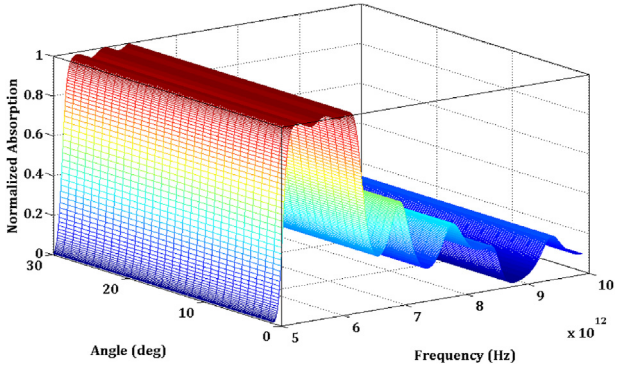

Figure 21. Absorption against different angles of the incident wave for wide-band mode (Mode B).

regarding two points. Firstly, it determines algorithm accuracy, the crowded population probably leads to more precise results. Secondly, it specifies the computational time. So, an important tradeoff exists for setting population size, accuracy against time-consuming. To numerically allocation genes, the simplest method is that the first gene set to initial value in the range and the last gene be equal to the final value in the specified range. In this way μ_{c1_1} set to 0 eV while μ_{c1_n} set to 1 eV. Similarly, d_1 is set to 5μm, and d_n is set to 95μm. Other genes' value is specified based on the initial value, final value, and population size according to Eq. (11).

$$Step\ \ Size\ =\ \frac{Final\ \ Value\ -\ \ Initial\ \ Value}{n} \tag{11}$$

5.2. The cross-over operation

To create new generations, cross-over between individuals is performed. There are numerous ways to produce a new generation. Here we consider a randomly based operation as tabulated in Table 3. Based on the table, a new individual consists of some genes from some individuals. It should be noted that the provided example is one probable state while parent individuals and selected genes are both randomly are chosen. For better vision, the child or new individual can be made of from two to five individuals randomly while selected genes can be chosen from any of parent individuals randomly. So, two random processes are involved in cross over the operation to reach the desired individual.

5.3. The mutation

To eliminate captivation on relative maximums, the mutation action is inevitable for a GA. Here the mutation is defined as two cascade

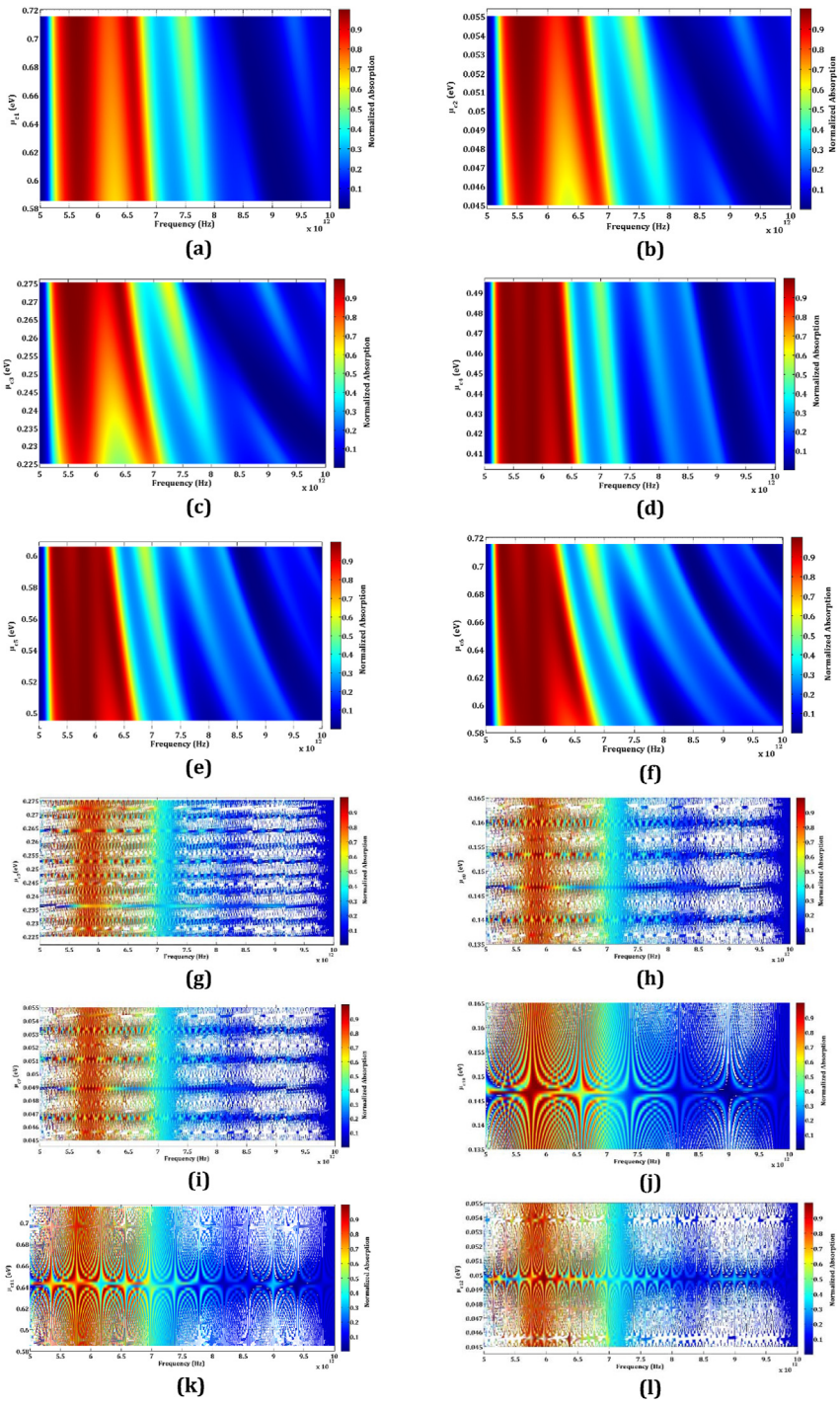

Figure 22. Absorption for 10 % variations of chemical potentials for wide-band mode (Mode B). Sub-Fig. (a) to Sub-Fig. (l) show absorption for μ_{c1} to μ_{c12} variations respectively.

Table 7. Comparison table.

Literature Refs	Operating Band (THz)	Number of Bands
[25]	0.1–2	2
[26]	0.5–0.9	1
[27]	1.2–2	2
[28]	0.01–0.1	2
[29]	0.15–0.85	2
This work	**5–10**	**6**

arbitrary steps. Initially, a gene is selected randomly and then multiply with a random number. Again, this stage with two random actions can help to avoid relative maximums. The process is explained by Table 4.

5.4. The defined cost-function

To specify the algorithm satisfaction, defining cost-function is inevitable. The major aim is maximizing the cost-function value. In this way, two separate cost-functions are presented for two desired absorption. Firstly, for multi-band absorption response, Eq. (12) is defined.

According to the definition, the cost function is a normalized absorption at several frequencies. 'A' denotes for absorption in a single frequency while 'n' noted the number of frequencies. Similarly, Eq. (13) is defined for absorption in a frequency range. Maximizing these equations means that used correspondence individuals have great potential to show perfect absorption. So related parameters can be extracted accordingly.

$$\begin{aligned} &C.F = \frac{A_1 + A_2 + \ldots + A_{n-1} + A_n}{n} \\ &A_n \rightarrow \textit{Absorption in } f_n \\ &n \rightarrow \textit{Number of frequencies} \end{aligned} \tag{12}$$

$$C.F. = \frac{1}{f_H - f_L}\int_{f_L}^{f_H} 1 - |\Gamma|^2 \, df \tag{13}$$

where:

$\Gamma = \frac{Z_{in} - Z_o}{Z_{in} + Z_o}$, and frequency range is $f_H - f_L$.

5.5. The impedance matching theory

The design process is based on the impedance matching theory. In this way, if the proposed device shows matched impedance with free space, so a perfect absorption occurs. If the matching occurs in single frequencies, we have a multi-band absorption response while matching over a frequency range leads to a wide-band absorption response. The absorption can be express as$A = 1 - |\Gamma|^2$, since the transmission channel is closed due to bottom golden plate. On the other hand, Γ is a function of the structure impedance while the impedance itself depends on structure geometry and chemical potentials.

6. Simulation results and discussion

Table 5 tabulates designed reconfigurable absorber with its geometries. Layers' thicknesses, disks radiuses, and periods are reported via the table. In accordance to ECM and the GA output in Table 5, full wave simulations are performed by CST Studio v.2019 in the frequency domain. A unit cell in the $x - y$ direction simulated while free space is assumed as z direction. Additionally, Table 6 includes chemical potentials corresponding to multi-band and wide-band absorptions. The interesting fact is the point that the proposed absorber with unique geometry can act as both multi-band and wide-band absorber which turns it an excellent choice for numerous applications.

First of all, impedance versus frequency is investigated. Figure 8 and Figure 9 are reported to show the impedance of both operational modes. As illustrated in Figure 8, the multi-band mode (Mode A) shows nearly complete impedance matching at three single frequencies (6 THz, 7 THz, and 8 THz). This means that the real part of impedance at these frequencies is about $120\pi\ \Omega$ with nearly zero imaginary section simultaneously. Similarly, Figure 9 demonstrates nearly perfect matching on a relatively wide frequency spectrum between 0.5 THz and 2.5 THz which is considered as Mode B. Target frequencies and the frequency range are specified in these figures with colored dashed line rectangular. The impedances are calculated via the mentioned ECM while Figure 10 verifies the performance accuracy of the exploited ECM with FEM simulation. This figure shows the absorption response for both operational modes. According to this figure Mode A expresses a multi-band absorption while changing gate biases according to Table 6, the device turns to Mode B as wide-band absorption. According to our investigations, the difference absorption response between the ECM and FEM simulation is less than 1 % regarding amplitude value with less than 100 GHz frequency shifts in some points. This difference is marginal and negligible for operation.

Besides, dependency on layers thicknesses (d_1, d_2, and d_3) for Mode A, is investigated via Figure 11, Figure 12, and Figure 13. Based on these figures, 10 % variations of layers thicknesses have negligible effects on the absorption response. So, it can be concluded that the proposed device is robust enough versus layers heights. Also, Figure 14 shows the absorption response against a 10 % variation of electron relaxation time. According to this figure, lower values of relaxation times exhibit more intense absorption which is compatible with its physics behind it [2]. Additionally, Figure 15 reveals absorption curves versus different incident angles. As it was predictable such a multi-layer and high height structure is relatively insensitive to angular radiations.

Moreover, Figure 16 is depicted to check out chemical potential's fluctuation on absorption response. According to this figure, twelve chemical potentials are changed 10 % from original values and corresponding absorptions are depicted accordingly. Based on these simulations μ_{c4}, μ_{c5}, and μ_{c6} have a larger influence on response compared to other chemical potentials. The reason behind this stems from the calculated impedance dependency on these parameters.

Finally, similar to Mode A, Figure 17, Figure 18, and Figure 19 shows absorption response versus layers thicknesses variations. Figure 20 reports absorption against electron relaxation time fluctuation while Figure 21 exhibits absorption response against variations of incident angles. Also, Figure 22 reports twelve absorption response corresponding to 10 %variations of twelve chemical potentials.

Finally, Table 7 compares our proposed absorber with prior reported devices.

7. Conclusion

A reconfigurable, graphene-based absorber is proposed in this paper. Exploiting a multi-bias scheme for graphene layers and an evolutionary algorithm, the device is designed with three layers. Two operational modes as wideband and multi-band absorptions are presented. Leveraging both method and concept, the designed absorber shows excellent robustness versus geometrical parameters. Also, ample simulations are performed to verify performance excellency. Based on obtained results, proposed structure perfectly absorbs THzincident radiation between 5.2 $THz - 6.3$ THzin wide-band mode while shows perfect absorption response in 5.3 THz, 7.5 THz, 8 THz, 8.5 THz, 9 THz, and 9.5 THzin multi-band operational mode. Also, response dependency to dielectric thicknesses, electron relaxation time, chemical potentials, and incident angles are considered to validate superior performance of proposed structure.

Declarations

Author contribution statement

Sindokht Cyrus: Performed the experiments; Analyzed and interpreted the data; Wrote the paper.

Sadegh Biabanifard: Conceived and designed the experiments; Performed the experiments; Contributed reagents, materials, analysis tools or data; Wrote the paper.

Funding statement

This research did not receive any specific grant from funding agencies in the public, commercial, or not-for-profit sectors.

Data availability statement

Data will be made available on request.

Declaration of interests statement

The authors declare no conflict of interest.

Additional information

No additional information is available for this paper.

References

[1] Yuping Zhang, et al., Optical properties of one-dimensional Fibonacci quasi-periodic graphene photonic crystal, Opt. Commun. 338 (2015) 168–173.
[2] K.S. Novoselov, A.K. Geim, S.V. Morozov, D. Jiang, Y. Zhang, S.V. Dubonos, Firsov Electric field effect in atomically thin carbon films, Science 306 (2004) 666–669.
[3] A.K. Geim, S.K. Novoselov, The rise of graphene, Nat. Mater. 6 (2007) 183–191.
[4] S.B. Parizi, B. Rejaei, A. Khavasi, Analytical circuit model for periodic arrays of graphene disks, IEEE J. Quant. Electron. 51 (2015) 1–7.
[5] Anna C. Tasolamprou, et al., Experimental demonstration of ultrafast THz modulation in a graphene-based thin film absorber through negative photoinduced conductivity, ACS Photonics 6 (3) (2019) 720–727.
[6] Shobhit K. Patel, et al., Broadband and efficient graphene solar absorber using periodical array of C-shaped metasurface, Opt. Quant. Electron. 52 (5) (2020) 1–19.
[7] Rui Xing, Shuisheng Jian, A dual-band THz absorber based on graphene sheet and ribbons, Opt Laser. Technol. 100 (2018) 129–132.
[8] David Keun Cheng, Field and Wave Electromagnetics, Pearson Education India, 1989.
[9] Iman Chaharmahali, Sadegh Biabanifard, Mahdi Mosleh, Graphene-based multi-layers THz absorber: circuit model representation, Optik (2020) 165596.
[10] Mohamadreza Soltani, et al., A configurable two-layer four-bias graphene-based THz absorber, J. Comput. Electron. (2020) 1–17.
[11] Alireza Najafi, et al., Reliable design of THz absorbers based on graphene patterns: exploiting genetic algorithm, Optik 203 (2020) 163924.
[12] Kamran Jafari Jozani, et al., Multi-bias, graphene-based reconfigurable THz absorber/reflector, Optik 198 (2019) 163248.
[13] Zanjani, Masoud Soltani, et al., A reconfigurable multi-band, multi-bias THz absorber, Optik 191 (2019) 22–32.
[14] Mohammad Biabanifard, et al., Analytical design of tunable multi-band terahertz absorber composed of graphene disks, Optik 182 (2019) 433–442.
[15] Sadegh Biabanifard, et al., Tunable ultra-wideband terahertz absorber based on graphene disks and ribbons, Opt. Commun. 427 (2018) 418–425.
[16] Biabanifard Sadegh, Ultra-broadband terahertz absorber based on graphene ribbons, Optik 172 (2018) 1026–1033.
[17] M. Biabanifard, et al., Design and comparison of terahertz graphene antenna: ordinary dipole, fractal dipole, spiral, bow-tie and log-periodic, Eng. Technol. 2 (2018) 555585.
[18] Sadegh Biabanifard, A graphene-based dual-band THz absorber design exploiting the impedance-matching concept, J. Comput. Electron. (2020) 1–11.
[19] Masoud Soltani-Zanjani, et al., Multi-bias graphene-based THz super absorber, Result Phys. 25 (2021) 104326.
[20] Toktam Aghaee, Ali A. Orouji, Circuit modeling of ultra-broadband terahertz absorber based on graphene array periodic disks, in: International Journal of Numerical Modelling: Electronic Networks, Devices and Fields, 2019, e2586.
[21] Toktam Aghaee, Ali A. Orouji, Reconfigurable multi-band, graphene-based THz absorber: circuit model approach, Result Phys. 16 (2020) 102855.
[22] Toktam Aghaee, Ali A. Orouji, Highly tunable multi-band THz absorber with circuit model representation using multi-bias scheme, in: International Journal of Numerical Modelling: Electronic Networks, Devices and Fields, 2020, e2777.
[23] Toktam Aghaee, Ali A. Orouji, Dual-band terahertz absorber based on graphene periodic arrays of disks and ribbons: circuit model approach, J. Comput. Electron. (2020) 1–15.
[24] Toktam Aghaee, Ali A. Orouji, Manipulating pattern periods via external bias for graphene-based THz dual-band Absorber, Microw. Opt. Technol. Lett. (2021) 1–11.
[25] X. He, S. Li, X. Yang, S. Shi, F. Wu, J. Jiang, High-sensitive dual-band sensor based on microsize circular ring complementary terahertz metamaterial, J. Electromagn. Waves Appl. 31 (1) (2017) 91e100.
[26] L. Cong, S. Tan, R. Yahiaoui, F. Yan, W. Zhang, R. Singh, Experimental demonstration of ultrasensitive sensing with terahertz metamaterial absorbers: a comparison with the metasurfaces, Appl. Phys. Lett. 106 (2015), 031107.
[27] F. Meng, Q. Wu, D. Erni, K. Wu, J. Lee, Polarization-independent metamaterial analog of electromagnetically induced transparency for a refractive-index based sensor, IEEE Trans. Microw. Theor. Tech. 60 (10) (2012) 3013e3022.
[28] C.-Y. Chen, I.-W. Un, N.-H. Tai, T.-J. Yen, Asymmetric coupling between sub-radiant and superradiant plasmonic resonances and its enhanced sensing performance, Opt Express 17 (17) (2009), 15372e15380.
[29] R. Yahiaoui, S. Tan, L. Cong, R. Singh, F. Yan, W. Zhang, Multispectral terahertz sensing with highly flexible ultrathin metamaterial absorber, J. Appl. Phys. 8 (2015), 083103.